UNSTEADY AERODYNAMIC MODEL OF A CARGO CONTAINER FOR SLUNG LOAD SIMULATION

João G. A. da Silva
Army/NASA Rotorcraft Division, Ames Research Center
Moffett Field, CA, USA.

Earl P. N. Duque
Dept. of Mechanical Engineering, Northern Arizona University
Flagstaff, AZ, USA

Luigi S. Cicolani
Army/NASA Rotorcraft Division, Ames Research Center
Moffett Field, CA, USA

Mark B. Tischler
Army/NASA Rotorcraft Division, Aeroflightdynamics Directorate, (AMRDEC)
U.S. Army Aviation and Missile Command
Moffett Field, CA, USA

Abstract

The problem of simulation models capable of predicting the aerodynamic instability of helicopter slung load cargo containers and bluff bodies is addressed. Instability for these loads is known to depend on unsteady frequency-dependent aerodynamics, but simulation models that include the unsteady aerodynamics do not currently exist. This paper presents a method for generating such models using computational fluid dynamics (CFD) to generate forced oscillation aerodynamic data and frequency domain system identification techniques to generate a frequency response from the CFD data and to identify a transfer function fit to the frequency response. The method is independent of the responsible flow phenomenon and is expected to apply to bluff bodies generally. Preliminary results are presented for the case of the 6 x 6 x 8 ft CONEX (container express) cargo container. The present work is based on 2D aerodynamic data for the CONEX sideforce and yaw moment generated by a forced oscillation in which frequency is varied smoothly over the range of interest. A first order rational polynomial transfer function is found adequate to fit the aerodynamics, and this is shown to provide a good match with flight test data for the yawing motion of the CONEX.

Nomenclature

a	speed of sound (ft/sec)
CD	drag coefficient
CS	side force coefficient
CN	yaw moment coefficient
I_{zz}	inertia about the body vertical axis (ft-lb-sec^2)
K_r	swivel friction coefficient (ft-lb-sec)
q	dynamic pressure (lb/ft^2)
r	yaw rate (1/sec)
s	Laplace transform variable
V	airspeed (kts)
α	angle of attack (deg)
β	sideslip angle (deg)
τ	time delay, time constant (sec)
ω	frequency (1/sec)

Introduction

Carrying underslung loads has long been one of the many applications of helicopters, both in military and civil operations. The load, however, introduces extra dynamics to the system, including potential load aerodynamic instabilities, which can reduce the speed envelope well below the power-limited speed of the aircraft-load configuration. Load-helicopter combinations are certified mostly by means of flight tests. Taking into account the diversity of possible loads (Ref 1) and the exploratory nature of the certification makes this procedure expensive, time consuming and sometimes dangerous. Therefore, simulations are a potentially efficient tool in the pre-evaluation of the flight envelope and the development of stabilization devices. To date, however, simulations have been inadequate in the case of cargo containers and other bluff bodies because the load aerodynamics have been based on static aerodynamics whereas stability for these loads has previously been shown to be due to unsteady aerodynamic effects (Refs 2, 3, and 4).

The modeling of unsteady aerodynamics associated with slung loads has been the subject of several studies, most of them carried out in the seventies and focused on the 8 x 8 x 20 ft MILVAN cargo container. In references 2 and 3 it was found that the use of quasi-steady derivatives alone was unsuccessful in predicting slung load instabilities, and that subjecting bluff bodies to forced oscillations yielded frequency-dependent aerodynamic coefficients. In references 2, 3, and 4 the cause of unsteady aerodynamic effects was identified with the existence of appreciable phase lags in the growth and

decay of separation bubbles and with vortex shedding. From these studies, it can be concluded that bluff body aerodynamics are comprised of the following components: static aerodynamics, viscous damping due to angular rates, unsteady aerodynamics of the stationary container due to vortex shedding, and unsteady aerodynamics of an oscillating container due to phase lags in separation bubble growth, and vortex shedding.

Two approaches have been taken previously in modeling unsteady load aerodynamics. The first approach, in work done at Northrop (Ref 4) and at the University of Bristol (Refs 2 and 3) and in reference 5, is to account for the observed oscillatory motions by introducing hysteresis in the moment function. This was based either on modeling the responsible flow phenomena (suction pressure distribution in the separation bubbles and lagged effects of angle rates), or on hypothesizing a model structure for the aerodynamic coefficients that reproduces the observed limit cycle oscillations and tuning the model parameters to the measured motions. The second approach, proposed in reference 6, is to identify the aerodynamic coefficients from forced oscillation input-output aerodynamic data. This approach makes no assumptions about the responsible flow phenomenon and can be applied to any load.

In this paper, the approach from reference 6 is adopted. The current effort benefits from the advent of computational fluid dynamics (CFD) codes that, after validation for the specific application, can rapidly provide considerable unsteady flow aerodynamic data compared to wind tunnel and flight test sources. The effort also benefits from frequency domain identification software that can generate frequency responses from time history data over the frequency range of interest and fit these responses with a model of the aerodynamics. The paper applies this approach to the 6 x 6 x 8 ft CONEX cargo container (Fig 1) which has been the subject of previous slung load studies, including flight testing (Ref 7), wind tunnel measurement of its static aerodynamics (Ref 8), and simulation studies (Ref 9). The goal of this work is to develop a modeling method, or model structure, that captures the unsteady aerodynamics of bluff bodies and can predict slung load instabilities. The present paper reports the initial results of that effort.

This paper first discusses the CFD method, the flow characteristics of the CONEX, and the forced oscillation inputs and corresponding aerodynamic outputs. Then the frequency responses are presented along with a discussion of the effects of amplitude, frequency, reference sideslip angle, and velocity. A transfer function model is defined and fitted to the responses and, finally, simulation results are given. The present study utilizes 2D

Fig. 1. UH60 – CONEX slung load configuration.

aerodynamics and focuses on the directional motions of the CONEX. The 2D aerodynamics suffice for estimates of side force and yaw moment, which are close to the 3D values, and also avoids the excessive computation time requirements for 3D unsteady flow computations. The lateral-directional degrees of freedom are thought to account for the instabilities of cargo containers.

Application of CFD to the CONEX

The prediction of unsteady aerodynamic forces on bluff bodies such as the CONEX requires time-accurate solution of the Navier-Stokes equations. A solution method must be able to accurately capture the viscous boundary layer flows as well as the unsteady and complex flow structures associated with vortex shedding. In addition, the method must have the ability to simulate dynamic body motions, either specified forced oscillations or due to aerodynamic forces.

The code chosen for this study is a Reynolds-averaged Navier-Stokes (RANS) solver known as OVERFLOW-D, version 1.5e (Ref 10). The OVERFLOW algorithm was first developed by Buning et al for fixed wing applications (Refs 11 and 12) and further developed by the U. S. Army for rotorcraft applications (Refs 13, 14, and 15). This code is suited to unsteady compressible flows and arbitrary body motions, as demonstrated in previous applications to unsteady rotorcraft blade motion and aircraft store separation simulations, and it can compute both 2D and 3D aerodynamics. Other algorithms that might be

considered for such unsteady separated flows include the Detached Eddy Simulation and the Large Eddy Simulation (Ref 16), but computation time requirements might be prohibitive for these codes.

Code options and parameter values related to integration schemes and dimensionless time step, grid extent and details, boundary conditions and turbulence model were selected for accuracy in the CONEX application. Details of these aspects of the computational setup will be reported separately.

All CFD computations were performed on the 32-processor Renewable Energy CFD Laboratory Compute cluster at Northern Arizona University. The code subdivides the system of overset grids among an appropriate number of the processors and passes boundary information between them in an efficient scalable manner using the Message Passing Interface libraries (Ref 17).

Computations

The CONEX is illustrated in Fig 2, along with its dimensions and the body axes orientation for this study. CFD computations were made for a rectangular box with the full-scale CONEX dimensions but omitting such CONEX details as skids and surface corrugations. The range of airspeeds of interest for the CONEX aerodynamic model is about 130 kts and below. The CFD computations were performed for Reynolds number 3.91 x 10^6 (which corresponds to the full scale CONEX at 60 kts with reference length 6.11 ft), and Mach number 0.2 (132 kts). The Mach number for the CFD work is an approximate minimum required to maintain solution accuracy for the current version of the compressible flow code. The aerodynamic coefficients are nearly invariant with Mach number over the speed range of interest for CONEX, and the variations with time can be scaled to other Mach numbers by scaling the dimensionless time of the CFD data to the desired Mach number, M, using:

$$t(M) = k\,\Delta\bar{t}(M_{CFD})\,\frac{M_{CFD}}{M}\,\frac{L}{a}$$

where t is real time, k is the time step index, $\Delta\bar{t} \equiv t\,L/a$ is the dimensionless time step used in the computations, a is the reference speed of sound, and L is the reference length. In addition, the aerodynamics of bluff bodies are generally expected to be nearly invariant with Reynolds number over the range of Reynolds numbers from wind tunnel models to full scale. This is demonstrated for the CONEX in Fig 3. The figure shows the power spectral density of the yaw moment coefficient for the 2D aerodynamics with the body at a fixed attitude ($\beta = 0$) vs reduced frequency or Strouhal number, $S_T = \omega L/V$, for three Reynolds numbers separated by 2 orders of magnitude and covering the range from wind tunnel models to full scale. Peaks occur at the frequency of the background vortex shedding of the unsteady flow and its harmonics. As seen, the Strouhal number for the peak is invariant with Reynolds number, and is identified as 0.70. A similar plot for Mach numbers (not shown) demonstrated a similar invariance with Mach number over the range of interest for the CONEX.

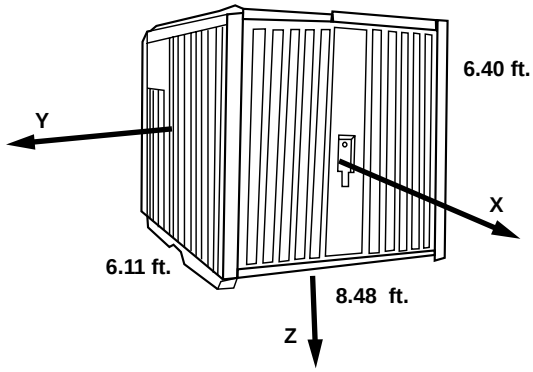

Fig. 2. CONEX.

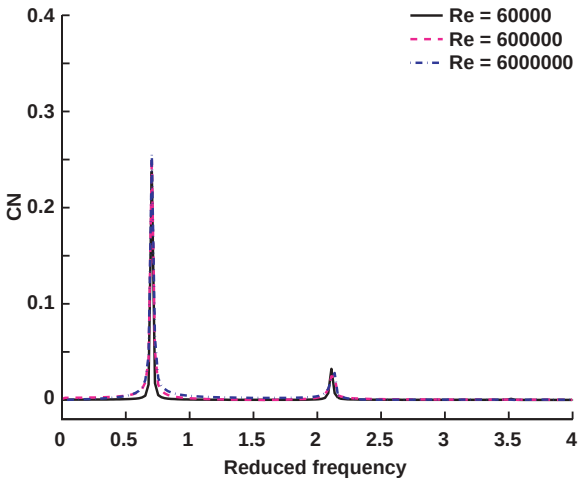

Fig. 3. Effect of Reynolds number on yaw moment frequency spectrum (2D aerodynamics).

The computational setup was validated by a comprehensive comparison of time-averaged results with wind tunnel data for the 3D static aerodynamics from reference 8. Validation of the vortex shedding frequency and other properties of the unsteady flow is desirable, but wind tunnel data for this were not available.

The CFD computations for this work included the static aerodynamics (2D and 3D) and 2D aerodynamic time history data for forced oscillations both at fixed frequencies and for frequencies varying smoothly over the range of interest (frequency sweep). The frequency sweep required 500,000 time steps. The 2D computations used 83000 grid points and required 50 CPU hours using two 1.8 GHz processors. The estimated time for 3D computations of the frequency sweep (1.5 million grid points, 8 processors) is 14.3 days at best. The development work of this paper is based on the 2D aerodynamics because of the difference in computation time and because the 2D directional aerodynamics suffice for the modeling objectives.

Flow Structure

Velocity contours for the flow around the horizontal center plane of the (3D) CONEX are shown in Fig 4. This illustrates the large separation bubbles that exist over the sides of the CONEX at zero sideslip and the massive wake extending downstream from the CONEX. At other orientations to the flow, the bubbles enlarge on the downstream side and reduce or disappear on the upstream side. Similar flow structures were documented for the MILVAN in the wind tunnel work in references 2 and 3. During oscillations, the flow structure lags the steady state structure corresponding to the instantaneous attitude, and there are corresponding lags in the aerodynamic forces and moments. For large enough oscillation amplitude, vortices are left behind at the rear corner of the downstream side as the CONEX retreats from the sideslip angle extreme, and this occurs at the frequency of the oscillation.

In addition, the (2D) wake is unsteady; that is, vortices are periodically shed into the wake alternately from the top and bottom rear corners, even when attitude is fixed. A snapshot of pressure contours in the extended wake is shown in Fig 5. A vortex “street” of successive pressure minimums marking the centers of vortices is clearly visible. The background vortex shedding occurs at a Strouhal number that is invariant with airspeed and was estimated at 0.70 for the CONEX (Fig 3). The corresponding physical frequency varies with velocity, as specified by its Strouhal number, and increases linearly with airspeed. The background vortex shedding results in continual oscillations of the aerodynamic coefficients at the vortex shedding frequency. Additional graphics and animations for both the static and oscillating CONEX can be seen in reference 18.

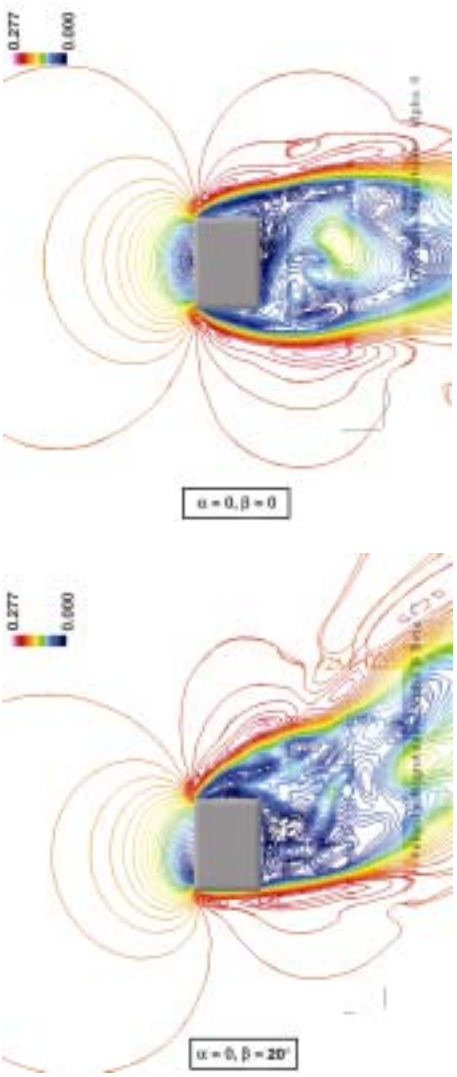

Fig. 4. CONEX Mach number contours (3D aerodynamics, fixed attitude).

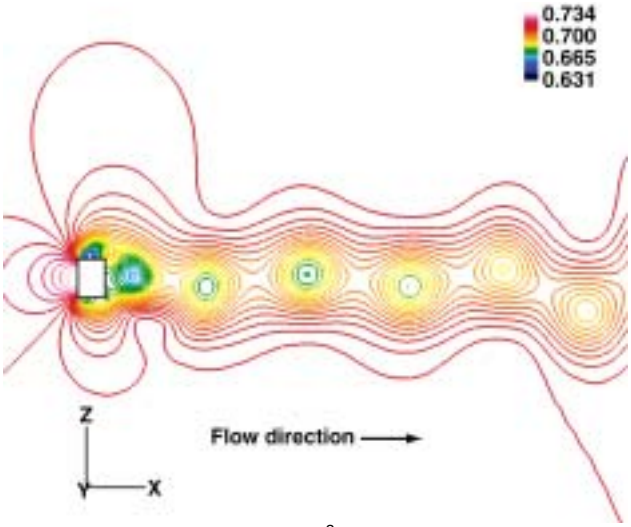

Fig. 5. CONEX pressure (p/pa^2) contours showing vortex street (2D flow).

2D vs 3D aerodynamics

The frequency response data used in the present modeling effort will use 2-dimensional aerodynamics for the x-y cross-section of the CONEX. A comparison of 2D CFD data and 3D wind tunnel data for the static aerodynamics is shown in Fig 6. There is good agreement in magnitude, zeros, and trends for yaw moment and moderate agreement for sideforce, while drag differs by a factor of about 1.7. A similar difference between 2D and 3D drag is known in the literature on flat plate aerodynamics, but this difference does not affect the present modeling effort that will consider only the unsteady sideforce and yaw moment

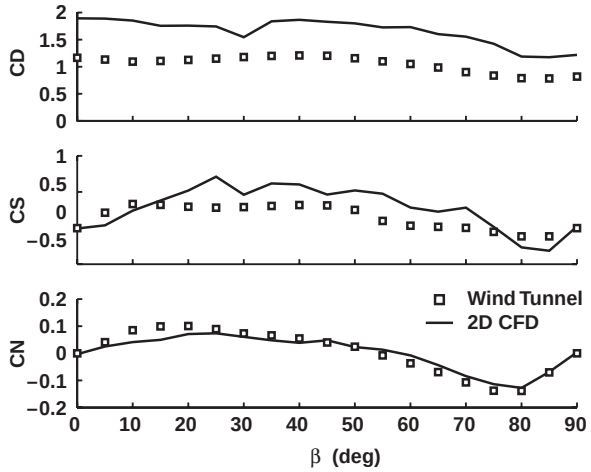

Fig. 6. Comparison of 2D CFD and 3D wind tunnel data ($\alpha = 0$).

Modeling Approach

Concept

In simulations, the aerodynamics model provides a relation between the flow variables (incidence angle of interacting body, velocity, air properties, etc.) and the aerodynamic forces and moments produced. To include the dynamic effects of unsteady flow, the aerodynamics of a body can be viewed like any other dynamical system, with outputs such as forces and moments, and with inputs such as incidence angles, flow velocity, density, temperature, etc. (Fig 7). In applications, the time scale separation between the flow dynamics and the driving inputs is usually large enough to consider the outputs as time invariant, thereby reducing the aerodynamics to a static problem. In some cases quasi-static terms dependent on input derivatives $\overset{o}{\alpha}, \overset{o}{\beta}, p, q, r$ are included. These are computed from behavior in the vicinity of zero rates. However, wind tunnel studies of bluff bodies have shown that static and quasi-static descriptions are insufficient to fully characterize their aerodynamics. This results from the nature of the flow around such bodies, which is dominated by massive separations involving large time scales. Thus, given the increase of the flow time scale towards that of the driving inputs, the aerodynamic forces and moments can no longer be considered time invariant. As wind tunnel studies indicate in the case of cargo containers, this is mainly reflected in the interaction between the incidence angle and the separation bubble growth, resulting in the latter lagging the motion. In this case, only the incidence angle varies in a time scale similar to that of the flow dynamics, whereas all the other inputs, such as velocity and air properties, vary slowly enough to be considered time invariant. The outcome is then a dynamic system affected by the time varying input vector $\theta(t)$, defining the incidence of the load, as well as by time invariant inputs defining the magnitude of the flow velocity V and the free-stream air properties.

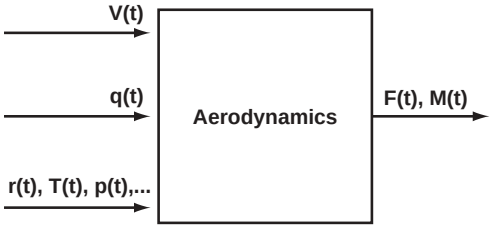

Fig. 7. General aerodynamic system.

Fig. 8. Directional aerodynamic system.

For this initial study of the problem, we further simplify from the 3D aerodynamic system (three input angles, six output force and moment components) to a 2D system that drives the slung load lateral-directional dynamics (Fig 8). This neglects some, but not all, of the aerodynamic couplings. Furthermore, given that the CONEX has a nearly cubic shape, then no significant changes are expected between the flow phenomena governing the aerodynamics of the lateral-directional and the longitudinal dynamics. The 2D system has a single input (sideslip) and three outputs (drag, sideforce, yaw moment), which require three independent input-output relations. Each of these relations can be represented in the frequency domain by a rational transfer function:

$$\frac{CD(s)}{\Delta\beta(s)} = T_{D,\beta} \quad \frac{CS(s)}{\Delta\beta(s)} = T_{S,\beta} \quad \frac{CN(s)}{\Delta\beta(s)} = T_{N,\beta}$$

In reference 6 a model for the 8 ft x 8 ft x 20 ft MILVAN cargo container was derived using limited wind tunnel data from reference 3. It was found that a rational transfer function with second order numerator and denominator

was adequate to represent the container aerodynamics throughout the frequency range of the data. The 2nd order transfer function has the form:

$$\frac{CN(s)}{\Delta\beta(s)} = \frac{a_2 s^2 + a_1 s + a_0}{b_2 s^2 + b_1 s + 1}$$

This can be transformed to the time domain and rearranged to the following differential equation:

$$CN(t) = a_0 \Delta\beta(t) + a_1 \dot{\Delta}\beta(t) + a_2 \ddot{\Delta}\beta(t) - b_1 \dot{C}N(t) - b_2 \ddot{C}N(t)$$

Collecting terms:

$$CN(t) = CN_\beta \Delta\beta(t) + CN_{\dot\beta} \dot{\Delta}\beta(t) + CN_{unsteady}$$

where $CN_{unsteady}$ denotes the yaw moment contribution due to unsteady aerodynamic effects from higher order angle derivatives and other terms:

$$CN_{unsteady} = CN_{\ddot\beta} \ddot{\Delta}\beta(t) - b_1 \dot{C}N(t) - b_2 \ddot{C}N(t)$$

Generally, the order of the transfer function is selected to minimize complexity while retaining adequate accuracy of fitting the available data. Derivatives with respect to yaw rate, r, are neglected in the model because there are no first order sources of these effects, such as a vertical tail, so that flow lag effects represented by the sideslip derivative can be assumed to dominate the quasi-static angular rate effects.

Procedure

An approach based on system identification in the frequency domain was taken in the present effort to model the dynamics associated with bluff body aerodynamics. The three principal steps in the procedure are (1) obtain the response of the system to excitation over the frequency range of interest, (2) extract a frequency response (Fourier transform) from the input and output time histories, and (3) fit a transfer function to the frequency response. This approach is commonly used in control system analysis. It can be applied to any dynamic system, and in the case of bluff body aerodynamics, it makes no assumptions about the responsible flow phenomena and can be applied to any type of load for which unsteady aerodynamics are important.

The identification procedure for the present work is depicted in Fig 9 and can be divided into five steps. First the input forced oscillation in sideslip angle is defined to excite the system over the desired frequency range and at an appropriate amplitude. This can be done using a set of fixed frequencies distributed over the desired frequency range, as has been done in wind tunnel studies, or using a single input time history in which the frequency varies continuously over the desired range (frequency sweep) as has been done in control system identification work. Second, this signal is used in the CFD simulation to generate the corresponding forced oscillation aerodynamic data. Third, the CFD output and the input signals are pre-processed to remove data anomalies (dropouts and wild points), to scale the data from the dimensionless time of the CFD computations to real time at the reference speed of the present study (60 kts), and to account for the inevitable differences between CFD and simulation conventions regarding axes, signs, reference areas, point about which moments are taken, etc.

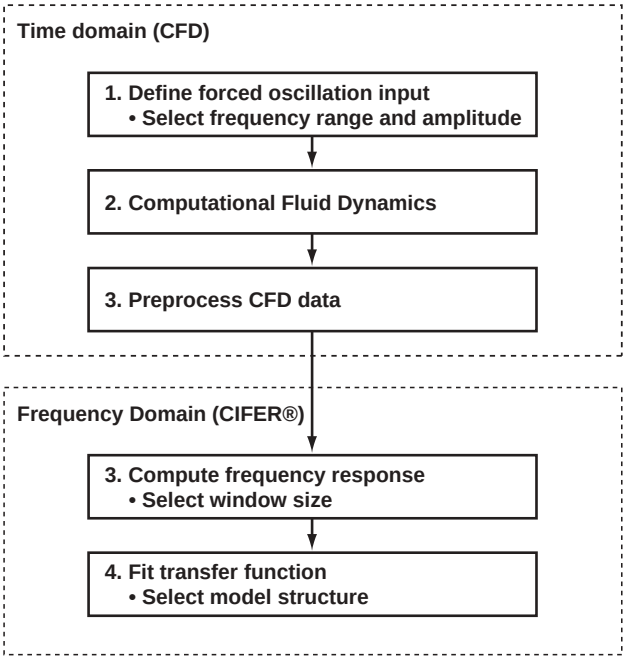

Fig. 9. Development procedure for unsteady aerodynamics model.

Fourth, the frequency responses are computed using Fourier transform methods. The CIFER® (Ref 19) software package for frequency domain analysis in aeronautical applications was used. The frequency response represents the first harmonic approximation of the input-output dynamics. The residual signal associated with the higher order harmonics is seen as noise in this approximation. The quality of the approximation is measured by the coherence function which is the linear correlation between input and output as a function of frequency and has values in the interval [0,1]. Values above 0.6 are considered necessary for credible frequency response results. Turbulence, uncorrelated or nonlinear dynamics all reduce the coherence function. A factor in the computations is the window size into which the Fourier analysis subdivides the time history. Results are better in particular frequency ranges according to the

window size, and responses for different windows can be computed and optimally combined by CIFER® to get the final frequency response.

The final step consists of fitting a transfer function to the frequency response, after selecting the transfer function model structure based on response complexity and physical insight.

Time History Data

Frequency Sweep

In a frequency sweep input, frequency is varied over the frequency range of interest using the equations (Ref 20)

$$\omega = \omega_{MIN} + C_2\left(e^{C_1 \frac{t}{t_{sweep}}} - 1\right)(\omega_{MAX} - \omega_{MIN})$$
$$\theta = \int \omega \, dt$$
$$\beta = \beta_o + A\sin(\theta)$$

Frequency varies exponentially from $\omega_{\min}$ to $\omega_{\max}$ during the time interval, t_{sweep}. The parameters C_1, and C_2 are empirically determined such that the coefficient factor in the equation varies from 0 to 1 over the sweep interval in a satisfactory way ($C_1 = 4$, $C_2 = 0.019$). An acceptable value for the sweep interval is 3 to 5 times the period of the minimum frequency. The forced oscillation angle β has amplitude A and varies about the mean angle β_o. The above equations were modified for the CFD computations in dimensionless time by replacing time and frequency with dimensionless time and reduced frequency.

The sweep gives uniform spectral content over the frequency range. This results in a smoother frequency response than can be obtained from a set of discrete frequencies distributed over the frequency range. In addition, the sweep requires only a single run that is only as long as would be required for a fixed frequency run at the lowest frequency for a sufficient number of cycles.

Sweep Amplitude

The choice of amplitude is a compromise between large enough amplitude to allow proper growth of the separation bubbles and excitation of the unsteady aerodynamics, and small enough amplitude to avoid regions of excessive nonlinearity of the aerodynamics. The static aerodynamics vs sideslip are shown in Fig 10 for reference. For example, the yaw moment coefficient reaches an extreme at 20° and then reverses itself to a minimum near 80°. Amplitudes of 10°, 20°, and 45° were considered. Frequency responses indicated that 20° amplitude provided reasonable linearity and good excitation of the unsteady aerodynamics, while 10° gave inadequate excitation and 45° encompassed excessive nonlinearity.

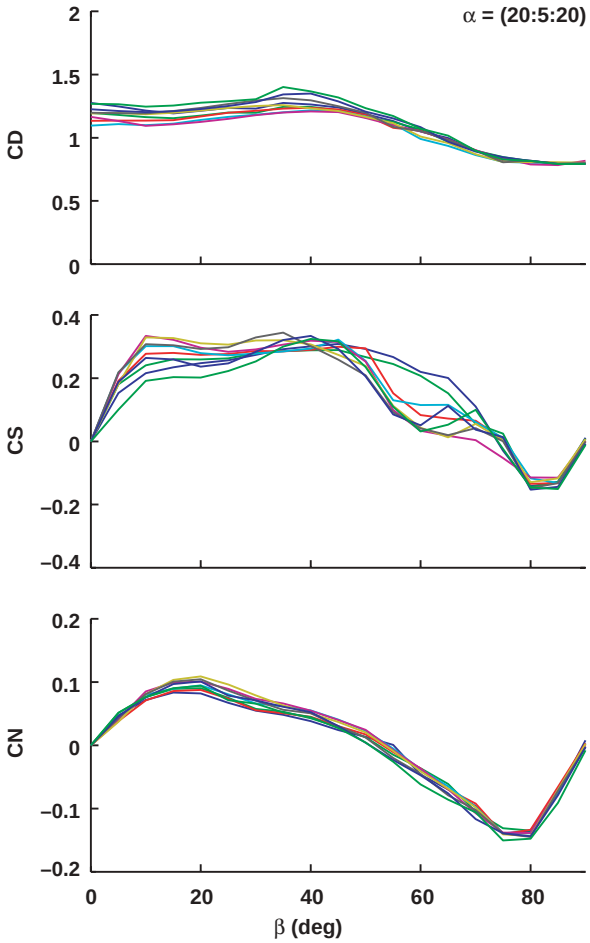

Fig. 10. CONEX static aerodynamics, wind tunnel data.

Frequency range and sample time history

The frequency range of the computations should include the vortex shedding frequency in order to capture the effect of the interference between body oscillations and the flow dynamics. Fig 11 shows the aerodynamic response (drag, sideforce, yaw moment coefficients) to a frequency sweep input around $\beta_o = 0$. The response exhibits two frequencies: (1) the frequency of the driving oscillation, and (2) a higher constant frequency associated with vortex shedding that is present independent of the input frequency. The oscillations due to vortex shedding are visible in greater detail in Fig 12, which shows the initial 10 sec interval from Fig 11 during which attitude is fixed. The drag coefficient oscillates at twice the vortex shedding and input frequencies owing to its symmetry about zero sideslip angle. (This would not be the case at other angles.) Amplitudes at the vortex shedding frequency are somewhat larger than amplitudes due to the 20° forced oscillation. The sideforce and yaw moment oscillations due to vortex shedding are, surprisingly, larger than the extreme values of the 3D static aerodynamics for these coefficients, but are consistent with the fluctuations seen in wind tunnel studies of square and rectangular cylinders (e.g., Ref 21). This suggests the possibility of significant differences between fluctuations for the 2D and 3D unsteady aerodynamics but this was not evaluated.

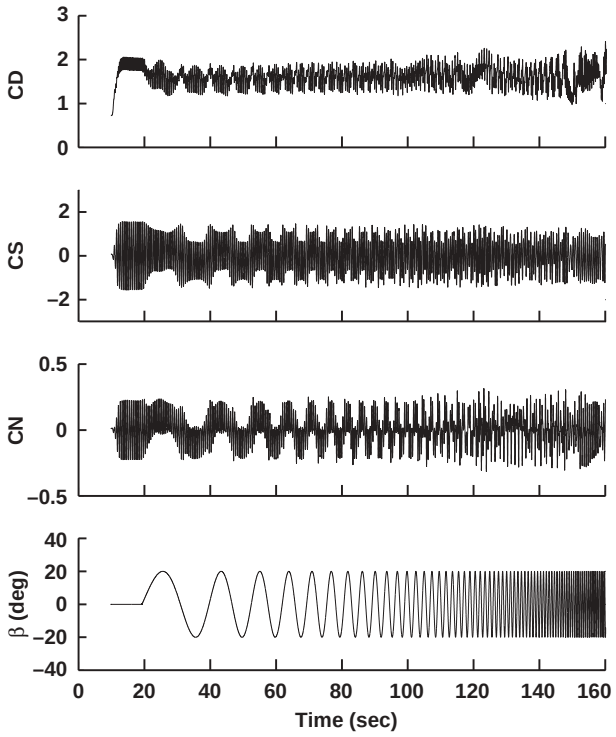

Fig. 11. Aerodynamic response to frequency sweep (β_o = 0, amplitude = 20°, 60 kts).

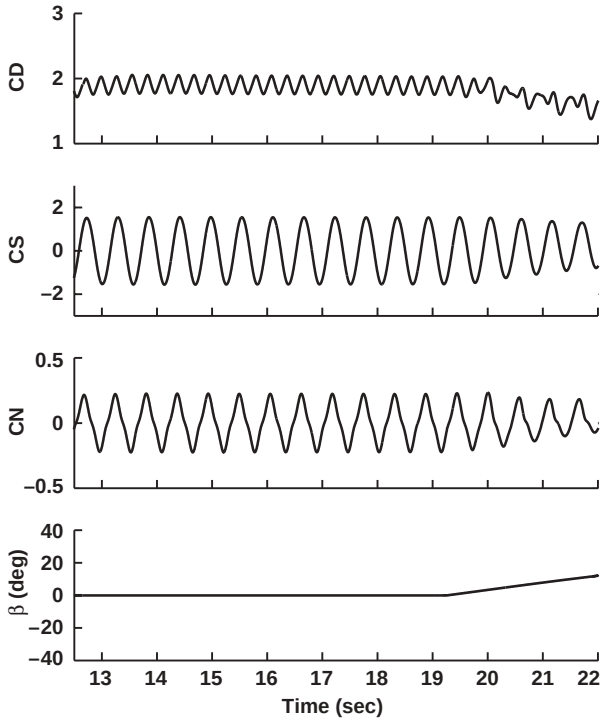

Fig. 12. Oscillations due to vortex shedding.

The data of Fig 11, correspond to a flow velocity of 60 kts at which the vortex shedding frequency is 11.3 rad/sec. This frequency varies with velocity such that the corresponding Strouhal number is invariant. The range of Strouhal numbers used in the forced oscillation was [0.014, 0.82] which includes the vortex shedding Strouhal number, 0.70. The corresponding range of frequencies at 60 kts is [0.25, 13.5] rad/sec.

In Fig 11, and in the remaining results the reference airspeed is 60 kts, input amplitude is 20°, 2D aerodynamics are used, the reference area and volume for the coefficients are the CONEX frontal area and volume, respectively, and moments are computed about the geometric center of the CONEX.

Frequency Domain Results

Transfer function fits (βo = 0, 60 kts)

The frequency response is a linear description of the response to oscillations around the reference sideslip angle. Frequency responses for CN, CS in the vicinity of β_o = 0 are shown in Fig 13. Responses were computed for five window sizes and these were combined optimally by CIFER® to get the final response. The smaller windows give better coherence at higher frequencies, and conversely, and the largest window defines the minimum frequency in the computed response. The largest window used should be no larger than 1/3 of the record length. In the result (Fig 13), the CN response loses adequate coherence at 9 rad/sec and above, while the CS response loses adequate coherence at 7 rad/sec and above.

Transfer function fits to the responses were made over the frequency range with adequate coherence. Coherence-weighted fits were generated with the CIFER® fitting utility. For CN it was found that first order numerator and denominator polynomials sufficed for a low cost fit owing to the flatness of the response. For the same reason there was poor separation of the first order numerator and denominator terms; that is, the cost of the fit had low sensitivity to large proportional changes in these two coefficients. However, the fit for CS gave negligible values of the first order numerator coefficient ($CS_{\substack{o \\ \beta}} \approx 0$) so that the denominator coefficient (time constant) was well determined. In the final computations, the CN and CS responses were fit simultaneously with the constraint that the denominator dynamics representing flow lags be identical, as they should be physically. Numerical values of the coefficients are given in the table (units are deg, sec). These values correspond to 60 kts. The transfer function can be extended analytically to other airspeeds as given in the next section.

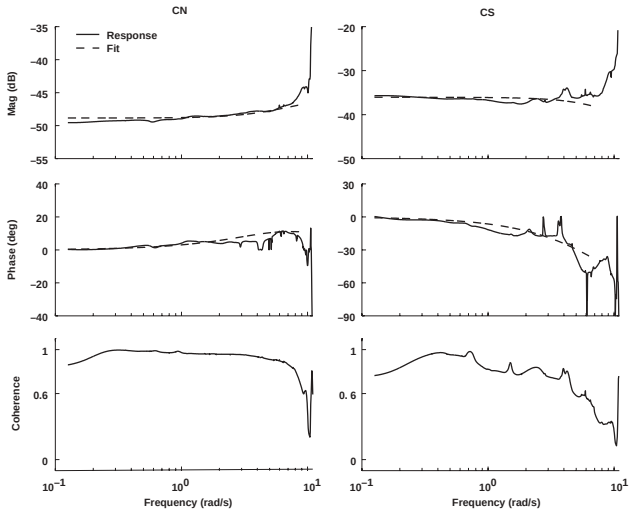

Fig. 13. Frequency response and transfer function fit; (β_o = 0, 60 kts).

Table 1. Transfer function model at β_o = 0, V = 60 kts

$\frac{CN(s)}{\Delta\beta(s)} = \frac{CN_{\beta_o} s + CN_\beta}{\tau s + 1}$			$\frac{CS(s)}{\Delta\beta(s)} = \frac{CS_{\beta_o} s + CS_\beta}{\tau s + 1}$	
τ	0.113		τ	0.113
CN_{β_o}	0.000602		CS_{β_o}	0
CN_β	0.00361		CS_β	0.0158
cost	7.7		cost	30.1

Frequency Response Near the Vortex Shedding Frequency

In the CN response around β_o = 0 (Fig 13) coherence drops below acceptable values for forcing frequencies above 9 rad/sec, so that behavior across the vortex shedding frequency at 12.4 rad/sec is poorly defined in these results. However, the available results capture the frequency dependence of CN up through 9 rad/sec satisfactorily. Several attempts to improve the high frequency coherence were made but were unsuccessful. The frequency sweep was revised to spend more time at high frequencies and a number of discrete frequency runs were made for frequencies distributed over the range (Refs 9 and 20) rad/sec. The discrete frequencies showed coherence near zero in the vicinity of the vortex shedding frequency, suggesting that there is little response to the forcing input compared to the independent vortex shedding effects at this frequency. Nevertheless, the computed response showed the expected 180° phase shift as the forcing frequency goes through the vortex shedding frequency.

Sideslip Offsets

Variations in the transfer function model with sideslip angle are of interest. Frequency responses for the yaw moment coefficient for reference sideslip angles every 30° in [0, 90°] are shown in Fig 14. Differences in magnitude at low frequencies reflect differences in the magnitude of the slope of $CN(\beta)$ at the reference angles, and the 180° differences in phase at low frequencies reflect the sign of the slope of $CN(\beta)$ in Fig 10. The responses at 0, 30°, and 60° are similarly flat with frequency but at 90° sideslip (short side facing the flow) the phase drops below –90° at high frequencies. This differs strongly from the phase behavior around 0° and implies large phase lags not present around 0°. Transfer functions were fit to each of these cases. At 30° and 60°, the best fits were obtained with time delay functions of the form, $(a_1 s + a_0)e^{-\tau s}$, while at 90° a second order rational polynomial was required. Details of these fits are omitted here. Although there are changes in the behavior of the coefficients with sideslip angle there are nevertheless some invariants. First, the time lag is approximately the same (0.113 sec) at all reference sideslip angles. In addition, the vortex shedding frequency was found to be invariant with sideslip angle.

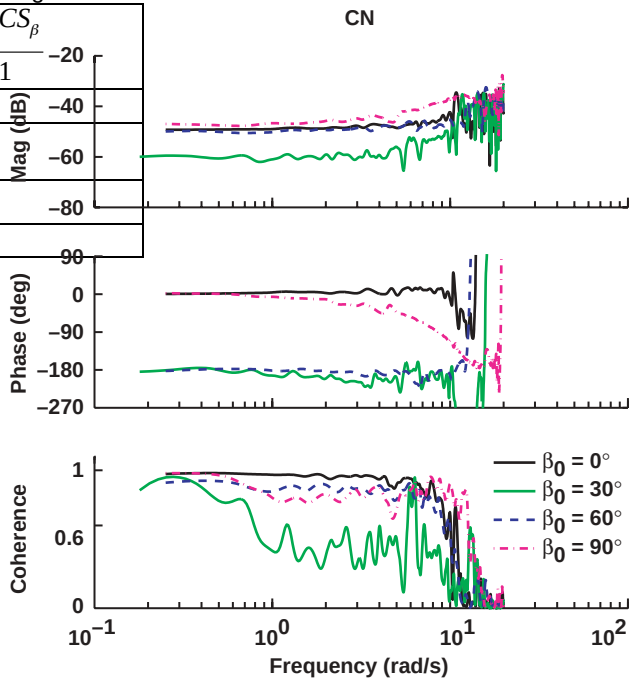

Fig. 14. Frequency responses for sideslip offsets 0, 30°, 60°, 90°, 60 kts.

Simulation

Yaw Motion Simulation

In some flight tests with the CONEX (Ref 7) the sling was attached at the hook with a swivel. With the swivel attachment, the CONEX spun up to a steady state yaw rate that increased with airspeed over the speed range of the tests. In this speed range, the yaw motions are decoupled from the pendulum motions and the pendulum modes are non-divergent. Consequently, a simple first test of the current model is to determine if it reproduces the

observed yaw motions in a one-degree-of-freedom simulation. Previous simulation studies using the load static aerodynamics (Ref 9) were able to reproduce the flight pendulum motions but failed to reproduce the divergent sideslip angle, which is driven by the unsteady aerodynamics. The decoupled yaw degree of freedom is represented by:

$$I_{zz}\,\dot{r} = q\,Vol\,CN(\beta,\dot{\beta},t) - K_r r$$
$$\dot{\beta} = -r$$

where the first term on the right is the aerodynamic yaw moment and the second term is swivel friction. Here, K_r was estimated at 1.245 ft-lbs-sec, *Izz* = 1376 ft-lbs-sec^2 for the flight test CONEX, *Vol* is the CONEX volume, and *q* is dynamic pressure.

The transfer function model for $CN(\beta,\dot{\beta},t)$ is given in the table above. This model can be modified to account for the nonlinearity of the static aerodynamics over large angle changes by replacing $CN_\beta\ \beta$ with the wind tunnel data, $CN^{WT}(\beta,\alpha)$ shown in Fig 10. In addition, the parameter values for the model given in the table correspond to 60 kts. At other airspeeds, the time dependence varies such that derivatives with respect to dimensionless time (t*V/L) are invariant. The final simulation model, valid at all airspeeds, is:

$$CN(V) = \frac{CN^{WT}(\beta,\alpha_o) + \frac{V_{ref}}{V} CN_{\beta_o}\, s\,\beta}{\frac{V_{ref}}{V}\tau\, s + 1}$$

where V_{ref} is the reference airspeed at which the coefficients were identified. Since this model applies in the vicinity of $\beta = 0$, it can be used for studies in which the CONEX is stabilized to trim at $\beta = 0$. However, the model will be applied at all β in the simulation tests described next. This approximation neglects changes in the higher order dynamics of the aerodynamics with sideslip, but captures the essential lag of the denominator dynamics at all sideslip angles.

The simulation was implemented using the MATLAB Simulink® utilities that conveniently implement transfer functions.

Results

Yaw rate response to offset initial conditions at 60 kts is shown in Fig 15. The baseline model for CN results in a neutrally damped non-divergent sideslip oscillation around zero. However, if the viscous damping ($CN_{\dot{\beta}_o}$) is removed, then the yaw rate is driven to a nonzero average steady state value, which represents a balance between swivel friction and destabilizing aerodynamic yaw moment due to the unsteady aerodynamics. After nulling the viscous damping, the swivel friction term was also adjusted to match the steady state yaw rate measured in the flight data. Thus, there is some interchangeability between viscous damping and swivel friction in this validation exercise. Attempts to measure the swivel friction directly were inconclusive.

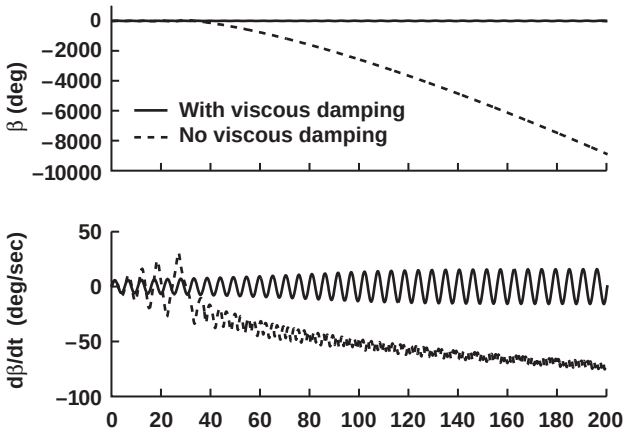

Fig. 15. Effect of viscous damping (60 kts).

Results were generated at other airspeeds over the range of the available flight data and yielded a similar response. A comparison of the simulation results for the steady state average yaw rate with the available flight data over the speed range from 20 to 65 kts is shown in Fig 16. These show good agreement with flight. Although the values of viscous damping and swivel friction are ambiguous in this test, the results show the potential of the model and the modeling approach to reproduce the flight yaw behavior both qualitatively and quantitatively.

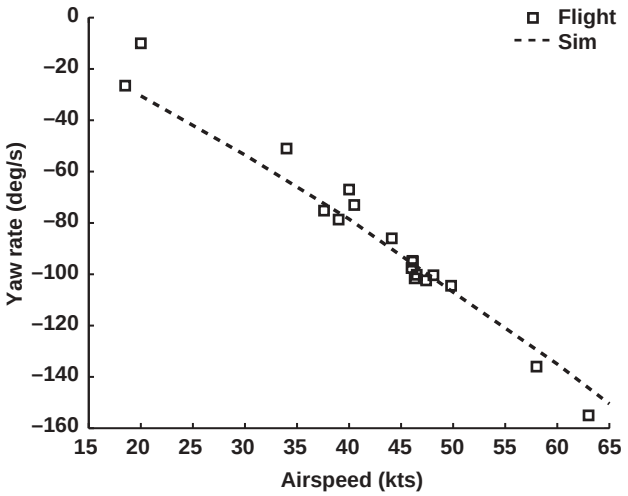

Fig. 16. Comparison of steady state yaw rate: simulation vs. flight.

Summary of Results

This paper has presented preliminary results from the combined use of CFD and system identification techniques to obtain a simulation model for the unsteady aerodynamics of the 6 x 6 x 8 ft CONEX cargo container. Detailed results from this study are:

1. The (2D) CONEX flow field at fixed attitude is characterized by separation bubbles along the sides with attitude-dependant geometry, and a massive wake which is unsteady owing to vortices that are regularly shed from the rear corners and at a reduced frequency which is invariant with Mach number and Reynolds number. During attitude oscillations, there are lags in the variation of the separation bubble structure, and vortices are shed at the frequency of the forced oscillation as a side retreats from its peak attitude.

2. The CFD computational setup was validated against 3D static aerodynamic wind tunnel data. Attempts to validate the background vortex shedding frequency and its effects on the coefficient dynamics were hampered by lack of wind tunnel data.

3. The present modeling work used 2D aerodynamics to reduce the CFD computation time requirements. It was found that the 2D sideforce and yaw moment (static) coefficients were close to the 3D values and suffice for simulation of the CONEX yaw dynamics in flight. However, possible significant differences between 2D and 3D unsteady flow effects on the coefficients remain to be evaluated.

4. The identification procedure views the aerodynamics as an unknown dynamic system in which the force and moment outputs are dependent on the frequency of the attitude inputs. The frequency sweep forced-oscillation input provides all the data needed to define the frequency response over the frequency range of interest in a single computational run. Input amplitude was selected to excite the flow lags sufficiently without including excessive nonlinearity of the aerodynamics. Frequency responses were well defined out to near the vortex shedding frequency but coherence was low around that frequency. This indicates a lack of input-output correlation at that frequency.

5. A transfer function fit of the frequency response for the nearly-cubic CONEX required only first order numerator and denominator to represent the aerodynamic response of the CONEX in the vicinity of zero sideslip angle (large face into the wind) with adequately small residuals. The model was extended analytically to speeds other than the reference speed of the identification, and was also modified to replace the linearized static stability term with the nonlinear static aerodynamics to account for large angles. Although the unsteady aerodynamic model was found to vary with sideslip angle, the time delay was approximately independent of sideslip.

6. A simulation of the CONEX yaw motions resulted in an excellent match to the yaw motions measured in flight in which the suspended CONEX spins up to a steady state average yaw rate that increases with airspeed. The match required tuning the aerodynamic model; the linear static aerodynamics were replaced with the nonlinear 3D static aerodynamics, and the higher order numerator dynamics (quasi-static derivatives) were neglected.

Important issues for further investigation include (1) the extension to a model for the 3-dimensional aerodynamics, (2) a method of accounting for variations in the dynamic model with sideslip angle, and (3) a demonstration that the model can predict the critical speed at which the underslung CONEX develops pendulum instability due to the aerodynamics.

Conclusions

The combined use of CFD computations and system identification techniques to obtain a simulation model for the unsteady aerodynamics of bluff bodies has been demonstrated. Theoretical models for the unsteady aerodynamics, which account for the load yaw motions and the instability of cargo container slung loads, are unknown. Once validated, CFD can generate generous amounts of aerodynamic coefficient data as well as comprehensive information on details of the flow. The identification procedure is based on forced attitude oscillation frequency sweep data over the frequency range of interest and results in a transfer function model of the dynamics, with order and parameter values to be determined from the data. This procedure is independent of the responsible flow phenomenon and can be applied to bluff bodies and slung loads generally. Application to the CONEX cargo container was successful in reproducing the load yaw motions seen in flight over the stable speed envelope of the CONEX.

References

1. Multiservice Helicopter External Air Transport. Vol I (basic operations), Vol II (Single point Load Rigging Procedures), Vol III (Dual Point Load Rigging Procedures). US Army FM-55-450-3,-4,-5. Feb 1991.

2. Chan, D., Flower, J., Simpson, A.: Aerodynamically Induced Motions of Bluff Bodies Suspended Beneath Helicopters. Final Report, Univ of Bristol, Dept of Aero Engr. Rpt AD. Oct 1975.

3. Simpson, A., Flower, J.: Unsteady Aerodynamics of Oscillating Containers and Application to the Problem of Dynamic Stability of HC Underslung Loads. AGARD CP-235, May 1978.

4. Watkins, T., Sincori, J., Kesler, D.: Stabilization of Externally Slung Helicopter Loads. USAAMRDL TR-74-42, Aug 1974.

5. Sampath, P.: Dynamics of a Helicopter-Slung Load System. PhD thesis. Dept Aerospace Eng, U. Maryland. April 1980.

6. Ronen, T.: Dynamics of a Helicopter with a Sling Load. PHD Thesis, Stanford Univ., Stanford, Ca, Aug 1985. Also T. Ronen, A. Bryson, W. Hindson: Dynamics of a Helicopter with a Sling Sload, Proceedings, AIAA AFM Conference, Aug, 1986.

7. Cicolani, L. S., McCoy, A. H., Sahai, R., Tyson, P. H., Tischler, M. B., Rosen, A., Tucker, G.: "Flight Test Identification and Simulation of a UH-60A Helicopter and Slung Load". *Journal of the American Helicopter Society*, Vol 46, No. 2, April 2001, pp 140-160.

8. Rosen, A., Cecutta, S., Yaffe, R.: "Wind Tunnel Tests of Cube and CONEX Models," Technion Institute of Technology, Dept of Aerospace Engineering, TAE 844, Nov 1999.

9. Tyson, P., et al: "Simulation Prediction and Flight Validation of UH-60A Black Hawk Slung Load Characteristics," 55th AHS Forum Proceedings, May 1999.

10. Meakin, R., Potsdam, M.: "Reference Guide for Scalable OVERFLOW-D, Version 1.5." May 2001, Ames Research Center, Moffett Field, CA. (restricted).

11. Buning, P. G., Chan, W. M., Renze, K. J., Sondak, D. L., Chiu, I-T., Slotnick, J. P.: "Overflow User's Manual, Version 1.6ab," Ames Research Center, Moffett Field, CA. Jan 1993, (restricted).

12. Palmer, J., Buning, P. G., Yanowitz, H., Venkatapathy, E.: "Three-Dimensional Computational Analysis of Complex Launch Vehicle Configurations." *Journal of Spacecraft and Rockets*, Jan-Feb, 1996, pp 49-53.

13. Meakin, R.: "Moving Grid Overset Grid methods for Complete Aircraft Tiltrotor Simulations," AIAA Paper 93-3350, July 1993.

14. Ahmad, J. and Duque, E.P.N.: "Helicopter Rotor Blade Computation in Unsteady Flows Using Moving Overset Grids," *Journal of Aircraft*, Vol 33, No. 1, Jan.-Feb. 1996, pp. 54-60.

15. Chan, W. M.: "The OVERGRID Interface for Computational Simulations on OVERSET Grids," 32nd AIAA Fluid Dynamics Conference, St.Louis Missouri, AIAA-2002-3188, June 2002.

16. Krajnovic, S., Davidson, L.: "Large Eddy Simulation of Flow Around a Three-Dimensional Bluff Body," 39th Aerospace Sciences Meeting, Reno NV, AIAA 2001-0432, Jan 2001.

17. MPICH: A Portable Implementation of MPI. Argonne National Laboratory, Argonne, IL, Jan, 2003. URL http://www-unix.mcs.anl.gov/mpi/mpich/

18. http://www.cet.nau.edu/~end2/Research/Rotorcraft/cube/mou_spr03/static.mpg and motion.mpg. July 2003.

19. Tischler, M. B., Cauffman, M. G.: "Frequency-Response Method for Rotorcraft System Identification: Flight Applications to BO-105 Coupled Rotor/Fuselage Dynamics", *Journal of the American Helicopter Society,* Vol 37, No. 3, July 1992, pp 3-17.

20. Tischler, M. B., Cauffman, M. G.: "Comprehensive Identification from Frequency Responses: An Interactive Facility for System Identification and Verification" Vol 1, NASA Conference Publication 10149, Moffett Field, CA, Sept 1994.

21. "ERCOFTAC Test Case LES2: Flow past a Long Square Cylinder". Univ. of Surrey, Guildford, U.K. Feb 1998. URL http://vortex.mech.surrey.ac.uk/LESig/les2/